Front tracking simulation of droplet displacement on solid surfaces by soluble surfactant-driven flows

Xinglong Shang,[1,2] Zhengyuan Luo,[3] Bofeng Bai,[3] Long He,[4] and Guoqing Hu[2,*]
[1]*Hangzhou Institute of Technology, Xidian University, Hangzhou 311200, China*
[2]*Department of Engineering Mechanics and State Key Laboratory of Fluid Power and Mechatronic Systems, Zhejiang University, Hangzhou 310027, China*
[3]*State Key Laboratory of Multiphase Flow in Power Engineering, Xi'an Jiaotong University, Xi'an 710049, China*
[4]*College of Mechanical and Electrical Engineering, Shaanxi University of Science and Technology, Xi'an 710021, China*

(Received 12 September 2023; accepted 8 December 2023; published 9 January 2024)

We provide comprehensive numerical insights into the displacement of droplets subject to soluble surfactant-driven flows. The effects of soluble surfactants on the dynamics of moving contact lines are introduced by the surfactant-dependent generalized Navier boundary condition. We show that surfactant transport significantly influences the displacement patterns of droplets on solid surfaces, affecting both the equilibrium state of the sliding motion and the critical conditions for detachment. In particular, a linear increase in the displacement velocity of a droplet with the dimensionless adsorption depth K is observed. This rate of increase is more pronounced at higher elasticity numbers, as evidenced by a more significant increase in the advancing contact angle. The critical condition for droplet detachment depends on the surfactant's ability to swiftly adsorb from the bulk and replenish at interfaces, which is improved as the Biot number Bi or K increases. Adsorption is enhanced by an increase in Bi, resulting in a decrease in the required time t_d for droplet detachment. However, this enhancement effect becomes nonmonotonic at high Bi values. In contrast, consistently increasing the bulk Peclet number decreases t_d, eventually approaching the convection limit where the Marangoni-induced drag force ceases to increase. In addition, surfactant transfer near the moving contact line at a moderate Damköhler number restricts the motion of the advancing contact lines, promoting droplet detachment. For all detachment scenarios, we find that detachment necessitates a critical effective capillary number, and an increase in this number results in an exponential decline in t_d.

DOI: 10.1103/PhysRevFluids.9.014002

I. INTRODUCTION

Droplet displacement on solid surfaces by another continuous fluid is a ubiquitous phenomenon observed in a wide range of applications such as coating [1], detergency [2], oil recovery [3], aircraft anti-icing [4], and water management in fuel cells [5]. The dynamics of the moving droplet, which may enter a steady sliding state and either partially or completely detach from the surface, is influenced by several factors. These include the applied external forces [6,7], the interfacial properties [8,9], the contact-line dynamics [10,11], and the properties of the surrounding

*Author to whom correspondence should be addressed: ghu@zju.edu.cn

fluid [12]. In these multiphase systems, where droplets are immersed in a liquid, surfactants are often added at the phase interface to drastically change the droplet dynamics, either in the bulk phases or in the droplets. These additives are often adsorbed at the phase interfaces and can profoundly affect the interfacial flow with moving contact lines (MCLs), making it difficult to predict the behavior of this complex multiphase system. The critical challenge is to accurately predict how the presence of surfactant affects droplet dynamics, with a quantitative account on surfactant adsorption−desorption kinetics, contact-line dynamics, and the fluid properties of the surfactant solutions. This detailed study would be very advantageous for understanding the role of surfactant in regulating interfacial flow and the mechanisms of surfactant-assisted droplet displacement.

Numerous experimental and theoretical studies have aimed to characterize the wetting dynamics of droplets containing surfactant solutions on different solid surfaces [13–15]. It has been observed that surfactants can dramatically change the kinetics of wetting and spreading, which depends on the surfactant transport and its effect on the surface tension and contact-line dynamics. In addition to the self-assembly of surfactant at the interphase interface, possible factors contributing to this mechanism include nonuniform surfactant distribution, Marangoni flow, and surfactant transfer through the MCLs, which play different roles in the dynamic wetting of individual droplets. Considerable experimental progress has been made in modeling MCLs in surfactant solution with moving deformable interfaces and providing reliable parameters for the model. However, certain aspects remain unexplored, including (i) the interplay between external field flow and soluble surfactant transport, which determines the flow- and time-dependent surface tension; (ii) the influence of the adsorption-desorption kinetics on the MCLs; (iii) the systematic investigation of droplet motion, deformation, and detachment and breakup. In particular, to account for the time and length scales of adsorption-desorption and convective-diffusive mass transfer in real experiments, it remains very challenging to obtain precise measurements of surface surfactant concentration, dynamic surface tension, and flow fields during the droplet displacement process. Numerical simulations can provide a closer look at the displacement process adjacent to the moving droplet and give further insight into how flow and surfactant-related parameters influence droplet dynamics on solid surfaces, which contributes to the understanding of the displacement mechanism, but the problem is very complicated to model.

To tackle the aforementioned challenges, available two-phase models have been made enabling the modeling of surfactant-laden flows with moving deformable interfaces. The efficient and accurate computational modeling of MCL dynamics with soluble surfactants still is a challenging task. In addition to the interface tracking and capturing for two-phase models, two key issues must be addressed, including the modeling of soluble surfactant transport and how it is incorporated into the MCLs [10]. Numerically, surfactants, owing to their small size, are usually represented by a continuous concentration field [16,17]. Typically, for the soluble case, two separate surfactant evolution equations must be solved together with the hydrodynamic equations at deforming interfaces and in the soluble phase [18]. To converse the surfactant mass, the surfactant evolution equations are coupled via a boundary condition involving adsorption and desorption kinetics. This complicated and nonlinear interaction with the flow field presents an additional numerical challenge. Consequently, a higher order scheme must be used in the spatial derivatives to obtain smooth solutions of the bulk concentration without any excessive oscillations near the interface for two-phase flows with large solubility ratios. Two-phase models for describing surfactant transport can be broadly categorized into two types based on the representation of the interface: front tracking (sharp interface) methods and front capturing (diffuse interface) methods. To compute surface gradients along the interface in a fixed Eulerian mesh, front capturing methods, such as volume of fluid (VOF) [19,20], level-set (LS) method [21,22], and phase-field method [23], generally extrapolate the concentration from the interface to the entire domain in the normal direction. From both the numerical and application points of view, these methods have the advantages of handling topological changes and using the same grid set to solve both the surfactant concentration evolution equations and the hydrodynamic equations. In particular, achieving surfactant mass conservation and the interface condition for the

surfactant evolution equation remain a challenge [24]. Several front tracking methods have been proposed for modeling surfactants, including the immersed boundary method [25], the front tracking method [26,27], and the boundary integral method [28]. Tracking a moving Lagrangian interface explicitly is recognized for its accurate mass conservation. Consequently, this type of method has a unique advantage for modeling interfacial mass transport, as the connectivity information of the neighboring element is tracked as the Lagrangian interface moves. A surfactant evolution equation can be directly discretized since interface connectivity can be effectively used to calculate the surface gradient term. A conservative scheme is necessary to maintain conservation of the total mass of surfactant at the deformed interface as it undergoes topological changes, i.e., breakup and coalescence [23,29]. Recently, a simple and robust topology changing algorithm has been presented in three dimensions in conjunction with the front tracking method [30]. This controllable algorithm in handling the topology changing process brings an advantage in simulating droplet dynamics with interphase interactions, which can explicitly impose the interface condition for mass exchange and complex interfacial mechanics, compared to other numerical methods such as the VOF and LS methods. However, for the more relevant case of soluble surfactants, there are still difficulties, particularly in describing the surfactant dynamics in the vicinity of the contact line.

When a droplet is displaced on a solid surface, the contact angle should vary dynamically with the surfactant transport [23]. A physical description of MCLs is complicated and remains only partially understood. From the numerical point of view, the complexity of contact-line dynamics makes the simulations very delicate. For instance, an infinite viscous dissipation with standard no-slip conditions induces the shear stress singularity at a moving contact line. This singularity has been mitigated by employing a slip boundary condition, e.g., the Naiver slip condition, or contact-line models [10]. In particular, these boundaries or semiempirical models straightforwardly impose the velocity or contact angle conditions associated with the initial interface configuration. Typically, these semiempirical models cannot be easily extended for surfactants without experimental data. A generalized Naiver boundary condition (GNBC) [31] is proposed as a complement to the Naiver slip boundary to describe the contact-line dynamics. It directly relates the slippage-induced friction on the solid surface to the slip velocity via a friction coefficient that controls the total amount of dissipation. This condition includes an uncompensated interfacial stress arising from a deviation from the equilibrium state, which can be influenced by the surfactant concentration via the Langmuir equation of state. To the authors' knowledge, only a handful numerical studies have been reported for interfacial flow with surfactants and MCLs [23,32]. However, most of these studies have either not considered the effect of the surfactant on the dynamics of MCLs or are one-way coupled to the external field. The integration of the surfactant-dependent condition for MCLs with efficient algorithms for handling topological changes makes front tracking methods a straightforward and intuitive approach for accurately modeling soluble surfactant-driven flows with MCLs.

In this paper, we extend our previous numerical scheme of the front tracking–finite-difference method to include soluble surfactants with MCLs. We use a front tracking method to explicitly track the deformed interface and the MCLs. The dynamics of the MCLs is resolved by the GNBC, leading to a slip velocity as a boundary condition at the solid surface to close the governing equations. We introduce the surfactant evolution equations for soluble surfactants in the bulk and at a deforming droplet interface. The surfactant exchange between the interface and the bulk occurs within a narrow adsorption layer adjacent to the interface and is modeled by a Langmuir adsorption-desorption kinetics. The surfactant adsorbed at the interface is distributed over the adsorption layer, causing the interfacial terms in the body force and GNBC to vary dynamically with the local surfactant concentration. In Sec. II, we outline the numerical methodology and validate the approach. The effects of the soluble surfactant on the deformation, motion, and detachment of the droplet on a solid surface are discussed in Sec. III. Finally, conclusions of the present work are drawn in Sec. IV.

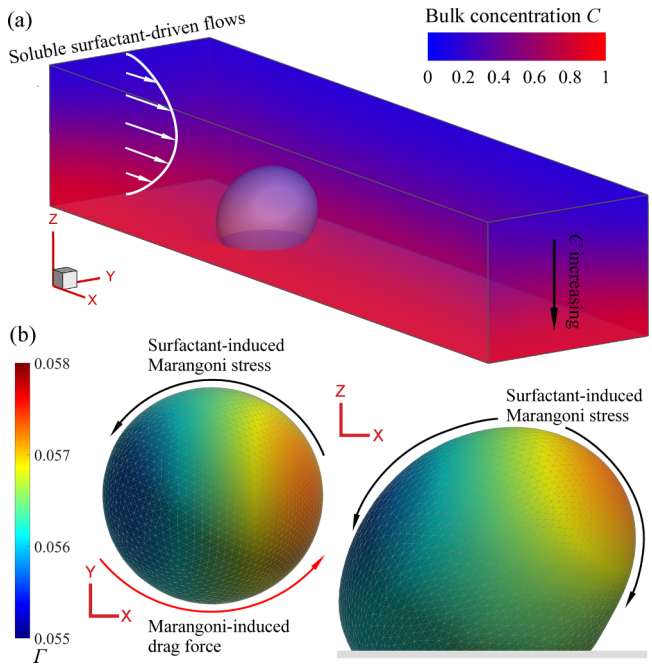

FIG. 1. (a) Schematic illustration of a liquid droplet adhering to a solid surface in a parabolic flow of surfactant solution of concentration C. The surface surfactant concentrations Γ due to the adsorption are shown in (b) and (c), respectively.

II. NUMERICAL METHODOLOGY

A. GNBC-based front tracking method

We introduce a surfactant-dependent contact-line model into the front tracking–finite-difference method to track the deformed droplet with moving contact lines (Fig. 1). A "one-fluid" formulation is used for the governing equations of two-phase flow. This approach employs a single set of equations to govern the entire computational domain with different material properties in each phase, and the surface tension term is included as a body force distributed in the region near the interface. The fluids inside and outside the droplet are incompressible, immiscible, and Newtonian, and both are governed by mass continuity and the Navier-Stokes equations,

$$\nabla \cdot \boldsymbol{u} = 0, \tag{1}$$

$$\frac{\partial(\rho \boldsymbol{u})}{\partial t} + \nabla \cdot (\rho \boldsymbol{u}\boldsymbol{u}) = -\nabla p + \nabla \cdot \mu(\nabla \boldsymbol{u} + \nabla \boldsymbol{u}^T) + \int_S (\nabla_s \sigma - 2\sigma\kappa \boldsymbol{n})\delta(\boldsymbol{x} - \boldsymbol{x}_f) ds. \tag{2}$$

Here, $\boldsymbol{u} = (u, v, w)^T$ is the velocity vector; t is the time; p is the pressure; and μ and ρ are the discontinuous viscosity and density, respectively. The last term in Eq. (2) represents the body force resulting from the interfacial tension force and the Marangoni stress in the presence of surfactants. Here, κ is the mean curvature, $\boldsymbol{n}$ is the outer unit vector normal to the interface, σ denotes the surface tension coefficient dependent on the local surfactant concentration, and s is the interface area. S represents the droplet surface. δ is a delta function with a nonzero value where $\boldsymbol{x} = \boldsymbol{x}_f$ wherein $\boldsymbol{x}_f$ and $\boldsymbol{x}$ denote the points at the interface and in the surrounding fluid, respectively. $\nabla_s = (\boldsymbol{I} - \boldsymbol{n}\boldsymbol{n}^T) \cdot \nabla$ is the surface gradient operator, where $\boldsymbol{I}$ is the identity tensor.

An indicator function I, which is zero in one phase and one in the other, is used to define fluid properties such as density and viscosity of the fluid on either side of the interface,

$$\rho = \rho_s + (\rho_d - \rho_s)I, \quad \mu = \mu_s + (\mu_d - \mu_s)I, \tag{3}$$

where ρ_d and μ_d are the density and viscosity of the droplet, respectively, and μ_s and ρ_s are the viscosity and density of the surfactant solution, respectively. The indicator function can be constructed by solving a Poisson equation related to the interface normal. A nonlinear equation of state is used to describe the relationship between the surfactant concentration and the surface tension,

$$\sigma = \max\left\{\sigma_c + R_g T \Gamma_\infty \ln\left(1 - \frac{\Gamma}{\Gamma_\infty}\right), \sigma_{\min}\right\}, \tag{4}$$

where σ_c is the surface tension coefficient of the clean surface, R_g is the ideal gas constant, T is the absolute temperature, Γ_∞ is the maximum packing concentration, and $\sigma_{\min}$ is the interfacial tension after reaching the critical micelle concentration, i.e., $\Gamma/\Gamma_\infty \approx 1$. Following the previous studies [27], we simply set $\sigma_{\min} = 0.05\sigma_c$ to avoid negative values of the surface tension.

The contact-line dynamics is modeled by imposing a slip velocity according to the GNBC [31], where the slip velocity $\boldsymbol{u}_{\rm cl}$ is proportional to the viscous shear stress $\tau^{\rm vis}$ on the solid surface and the unbalanced Young's stress $\boldsymbol{\tau}^{\rm Young}$ near the contact line:

$$\beta \boldsymbol{u}_{\rm cl} = \tau^{\rm vis} + \tau^{\rm Young}. \tag{5}$$

Here, β is the friction coefficient of fluid at the solid surface. In the present study, β is taken as a constant without accounting for the variations in fluid properties across the contact line. As we explicitly track the interface, it is relatively straightforward to calculate the unbalanced Young's stress, which depends on the surface tension and dynamic contact angles. We follow a similar procedure to implement the unbalanced Young's stress using a delta function, as used in the front tracking method, but for the two-dimensional case at the contact-line surface [33]. A slip velocity including the contact angle condition can be obtained and then used as a boundary condition to solve the governing equations (1) and (2). Ignoring the adsorption of the surfactant on the solid surface and the effect of surfactant on the equilibrium contact angle, the unbalanced Young's stress can be rewritten as

$$\tau^{\rm Young} = \int_L \boldsymbol{n}_{\rm cl}(\sigma_c \cos\theta_{\rm eq} - \sigma \cos\theta_d)\delta(\boldsymbol{x} - \boldsymbol{x}_{\rm cl})dl. \tag{6}$$

Here, $\theta_{\rm eq}$ and θ_d are the equilibrium and dynamic contact angles, respectively, dl is the length of a short segment of the contact line. $\boldsymbol{n}_{\rm cl}$ is the unit outer normal of the two-dimensional contact line, and $\boldsymbol{x}_{\rm cl}$ is the point on the contact line. Once the governing equation for the flow field is solved on the Eulerian mesh, the interface including the contact line is advanced by the following equations:

$$\frac{d\boldsymbol{x}_f}{dt} = \boldsymbol{u}_f, \tag{7}$$

where the interface velocity $\boldsymbol{u}_f$ is interpolated from the Eulerian velocity, except at the contact lines where its velocity is calculated directly using Eq. (5).

Surfactants are only soluble in the bulk fluid and can be adsorbed or desorbed at the droplet interface. Surfactant concentration at the deforming interface is governed by the time-dependent convection-diffusion equation:

$$\frac{\partial \Gamma}{\partial t} + \nabla_s \cdot (\Gamma \boldsymbol{u}_s) + \Gamma(\nabla_s \cdot \boldsymbol{n})(\boldsymbol{u} \cdot \boldsymbol{n}) = D_s \nabla_s^2 \Gamma + S_\Gamma, \tag{8}$$

where D_s is the surface diffusion coefficient of the surfactant and $\boldsymbol{u}_s$ is the tangential velocity at the interface. The source term S_Γ represents the mass exchange of surfactant between the interface and the adjacent bulk fluid. The surfactant exchange is assumed to occur only in a thin adsorption layer

adjacent to the droplet interface. The net accumulation rate of surfactant on the interface is equal to its adsorption rate minus its desorption rate,

$$S_\Gamma = k_a C_S(\Gamma_\infty - \Gamma) - k_d \Gamma, \tag{9}$$

where k_a and k_d are the adsorption rate and the desorption rate, respectively. C_S is the bulk surfactant concentration near to the interface.

The surfactants are only transported in the bulk phase, and at its boundaries, including the droplet interface. Following the technique proposed by Muradoglu and Tryggvason [27], we distribute S_Γ over the adsorption layer and add it to the bulk concentration equation as a negative source term S_C:

$$\frac{\partial C}{\partial t} + \boldsymbol{u} \cdot \nabla C = \nabla \cdot (D_I \nabla C) + S_C. \tag{10}$$

Here, D_I is defined as $D_I = D_c(1-I)$, where D_c is the bulk diffusion coefficient. The addition of surfactants is intended to modify the surface properties of the droplets and affects the material properties of the bulk fluid. According to the previous studies [34,35], the viscosity and density of the surfactant solution increase linearly with the concentration,

$$\rho_s = \rho_0 + (\rho_\infty - \rho_0)C, \tag{11}$$

$$\mu_s = \mu_0 + (\mu_\infty - \mu_0)C, \tag{12}$$

where μ_0 and ρ_0 are the viscosity and density of the bulk fluid without surfactant, i.e., $C = 0$, and μ_∞ and ρ_∞ are the viscosity and density of the surfactant solution at $C = C_\infty$.

B. Nondimensionalization

All the quantities in the equations are solved in their dimensionless forms by scaling the characteristic quantities as follows:

$$\tilde{\boldsymbol{x}} = \frac{\boldsymbol{x}}{R}, \quad \tilde{\boldsymbol{u}} = \frac{\boldsymbol{u}}{U}, \quad \tilde{t} = \frac{t}{R/U}, \quad \tilde{p} = \frac{p}{\rho_0 U^2}, \quad \tilde{\kappa} = \kappa R, \quad \tilde{\rho} = \frac{\rho}{\rho_0}, \quad \tilde{\mu} = \frac{\mu}{\mu_0}, \quad \tilde{\sigma} = \frac{\sigma}{\sigma_c},$$
$$\tilde{\lambda} = \frac{\lambda}{R}, \quad \tilde{\Gamma} = \frac{\Gamma}{\Gamma_\infty}, \quad \tilde{C} = \frac{C}{C_\infty}, \quad \tilde{C}_S = \frac{C_S}{C_\infty}. \tag{13}$$

The dimensionless material properties can be summarized as follows:

$$\frac{\rho_d}{\rho_0}, \quad \frac{\mu_d}{\mu_0}, \quad \frac{\rho_\infty}{\rho_0}, \quad \frac{\mu_\infty}{\mu_0}. \tag{14}$$

The dimensionless numbers are defined as

$$\mathrm{Re} = \frac{\rho_0 U R}{\mu_0}; \quad \mathrm{Ca} = \frac{\mu_0 U}{\sigma_c}; \quad \mathrm{Pe}_b = \frac{UR}{D_b}; \quad \mathrm{Pe}_s = \frac{UR}{D_s};$$
$$K = \frac{k_a C_\infty}{k_d}; \quad \mathrm{Bi} = \frac{k_d R}{U}; \quad \mathrm{Da} = \frac{\Gamma_\infty}{\mathrm{RC}_\infty}; \quad \beta_s = \frac{R_g T \Gamma_\infty}{\sigma_c}, \tag{15}$$

where $R = (0.75\,V/\pi)^{1/3}$ is the equivalent droplet radius based on its volume V, and C_∞ is the uniform far-field concentration. Re, Ca, Pe_c, Pe_s, K, Bi, Da, and β_s are the Reynolds number, the capillary number, the Peclet number based on bulk diffusivity, the Peclet number based on interfacial diffusivity, the dimensionless adsorption depth, Biot number, Damköhler number, and the elasticity number, respectively.

The tildes are dropped henceforth with the understanding that hereafter all variables discussed in the following sections are dimensionless unless otherwise stated. Thus, the dimensionless governing

TABLE I. Parameter definitions and ranges in our simulations.

Parameter	Range
$\mathrm{Re} = \rho_0 U R/\mu_0$	Fixed at 0.1
$\mathrm{Ca} = \mu_0 U/\sigma_c$	0.04–0.16
$\beta_s = R_g T \Gamma_\infty/\sigma_c$	0.2, 0.5
$\mathrm{Pe}_b = UR/D_b$	$0.01-10^4$
$\mathrm{Pe}_s = UR/D_s$	0.1, 1, 10
$K = k_a C_\infty/k_d$	0.1–1
$\mathrm{Bi} = k_d R/U$	0.01–10
$\mathrm{Da} = \Gamma_\infty/RC_\infty$	0.01–0.5
ρ_d/ρ_∞	Fixed at 0.9
μ_d/μ_∞	Fixed at 2
ρ_∞/ρ_0	Fixed at 2
μ_∞/μ_0	1, 2, and 4

equations become

$$\nabla \cdot \boldsymbol{u} = 0, \tag{16}$$

$$\frac{\partial(\rho \boldsymbol{u})}{\partial t} + \nabla \cdot (\rho \boldsymbol{u}\boldsymbol{u}) = -\nabla p + \frac{1}{\mathrm{Re}} \nabla \cdot \mu(\nabla \boldsymbol{u} + \nabla \boldsymbol{u}^T) + \frac{1}{\mathrm{ReCa}} \int_S (\nabla_s \sigma - 2\sigma\kappa \boldsymbol{n})\delta(\boldsymbol{x} - \boldsymbol{x}_f) ds, \tag{17}$$

$$\frac{\partial C}{\partial t} + \boldsymbol{u} \cdot \nabla C = \frac{1}{\mathrm{Pe}_b} \nabla \cdot (\nabla C) - \mathrm{Da} \int_S \mathrm{Bi}[KC_s(1-\Gamma) - \Gamma]\delta(\boldsymbol{x} - \boldsymbol{x}_f) ds, \tag{18}$$

$$\frac{\partial \Gamma}{\partial t} + \nabla_s \cdot (\Gamma \boldsymbol{u}_s) + \Gamma(\nabla_s \cdot \boldsymbol{n})(\boldsymbol{u} \cdot \boldsymbol{n}) = \frac{1}{\mathrm{Pe}_s} \nabla_s^2 \Gamma + \mathrm{Bi}[KC_s(1-\Gamma) - \Gamma], \tag{19}$$

$$\sigma = \max\{1 + \beta_s \ln(1-\Gamma),\ 0.05\}. \tag{20}$$

They are supplemented by the following velocity boundary conditions:

$$\boldsymbol{u}|_{x=0} = \left[4\left(1 - \frac{z}{L_z}\right)\frac{z}{L_z},\ 0,\ 0\right], \quad \boldsymbol{u}|_{z=L_z} = 0, \tag{21}$$

$$\boldsymbol{u}|_{z=0} = \boldsymbol{u}_{\mathrm{cl}} = \lambda \left.\frac{\partial \boldsymbol{u}}{\partial n}\right|_{\mathrm{wall}} + \frac{1}{\mathrm{Ca}}\frac{\lambda}{\mu} \int_L \boldsymbol{n}_{\mathrm{cl}}(\cos\theta_{\mathrm{eq}} - \sigma\cos\theta_d)\delta(\boldsymbol{x} - \boldsymbol{x}_{\mathrm{cl}}) dl, \tag{22}$$

and the concentration boundary conditions,

$$\left.\frac{\partial C}{\partial z}\right|_{z=0} = \left.\frac{\partial C}{\partial z}\right|_{z=L_z} = 0, \quad C|_{x=0} = \frac{1}{L_z}(L_z - z). \tag{23}$$

The computational domain size is $L_x \times L_y \times L_z$ in the x, y, and z directions, respectively. The boundary conditions are periodic in the y direction. In addition, the diffusive flux of surface surfactants at the contact line is zero. Initially, the droplet is placed in a quiescent liquid and the bulk surfactant concentration is $C|_{t=0} = (L_z - z)(1-I)/L_z$. A uniform concentration $\Gamma|_{t=0} = 0.05$ is set to avoid negative values of the bulk surfactant concentration at the initial time. The ranges of the parameters are given in Table I unless otherwise specified.

C. Numerical implementation

To track the deformed droplet with the moving contact line, a three-dimensional GNBC-based front tracking–finite-difference method is used. This method has been used to study the dynamics of clean droplets on the solid surface [36,37], and it has been developed to model the interfacial

flow covered with insoluble surfactants [38]. These studies detail the numerical implementation of the GNBC in the front tracking method. This section only provides a brief overview of the front tracking method and elaborates on the numerical implementation for moving contact lines with soluble surfactants. The flow governing equations are solved using the three-stage Runge-Kutta–Crank-Nicolson four-step projection method on a stationary collocated uniform Cartesian grid [39]. A second-order central finite-difference scheme is used to approximate the spatial derivatives. The semi-implicit Crank-Nicholson technique is employed to update the diffusion term. The three-stage Runge-Kutta method is employed for the convective and body force terms in Eq. (2). A four-level V-cycle multigrid algorithm and the alternating direction implicit scheme are used to solve the pressure Poisson equation. An Adams-Bashforth scheme is employed to advance the interface by Eq. (7) including the contact lines.

The surfactant concentration at the deforming interface is solved on the triangular Lagrangian grid according to Muradoglu and Tryggvason [27]. The surface surfactant concentration is stored at the center of the triangular elements, where its evolution is solved using the finite volume scheme. Time integration is performed using an explicit Euler scheme. The three-stage Runge-Kutta method is also applied to solve the bulk concentration equations. To significantly reduce the numerical diffusion, we use a fifth-order weighted essentially nonoscillatory scheme to evaluate the convective term [27]. The source term S_Γ is first calculated on the Lagrangian mesh and is then distributed to the adjacent Eulerian meshes in the bulk phase. Surfactant adsorption and desorption at the solid surface is ignored and an impermeable boundary condition is imposed (see Appendix A). To satisfy the conservation of the surfactant during the distribution from the interface front to the Eulerian meshes, S_f in Eq. (32) is reformulated as $S_f = \sum_{i,j,k} D(\boldsymbol{r})$ if $I > 0.5$. $D(\boldsymbol{r})$ is a non-normalized distribution function (see Appendix B). As the interface deforms, the front is restructured by dynamically adding and deleting the element, while ensuring that the droplet volume and the surfactant absorbed on it are strictly conserved.

D. Model validation

To ensure the accuracy of the numerical method, a convergence study was carried out to test the effects of Eulerian and Lagrangian resolutions on the displacement of droplets with insoluble surfactant (see Appendix C). To ensure that the final state of a moving droplet is not affected by the grid resolutions, we have confirmed that the number of Eulerian grids per unit length R must exceed 20. In addition, 4608 Lagrangian grids are sufficient at the initial time to track the droplet detachment process. At this resolution, the loss of total surfactant mass adsorbed on the droplet surface is limited to less than 0.2%. The diffusion of the bulk surfactant and the mass exchange between the bulk and the interface are further validated in this section. Consider a clean droplet (i.e., $\Gamma|_{t=0} = 0$) with an equilibrium contact angle of $\theta_{\mathrm{eq}} = 90^\circ$ immersed in a quiescent solution with a uniform concentration $C|_{t=0} = C_\infty$. The computational domain $L_x \times L_y \times L_z = 10 \times 10 \times 5$ is discretized using a uniform $240 \times 240 \times 120$ Cartesian grid. The source term in Eq. (9) is reduced to $S_\Gamma = k_a C_s$ to ensure that the surfactant only adsorbs from the bulk phase to the droplet interface. An approximate solution for the bulk concentration C was given by Muradoglu and Tryggvason [40]:

$$\frac{C}{C_\infty} = 1 - \frac{\omega\chi\sqrt{t}}{1+\eta}\frac{a}{r}\mathrm{erfc}\left(\frac{r-a}{2\sqrt{D_s t}}\right), \tag{24}$$

where $\mathrm{erfc}(r)$ is the complementary error function, r is the distance to the center of the droplet, a is the radius of the droplet, $\omega = k_a/D_s$, $\chi = \sqrt{\pi D_s}$, and $\eta = \chi(1+\omega a)/a$. The surface surfactant concentration Γ is then given by

$$\Gamma = \Gamma|_{t=0} + k_a C_\infty\left(t - \frac{\omega\chi}{\eta^3}(\eta^2 t - 2\eta\sqrt{t} + 2\ln(1+\eta))\right). \tag{25}$$

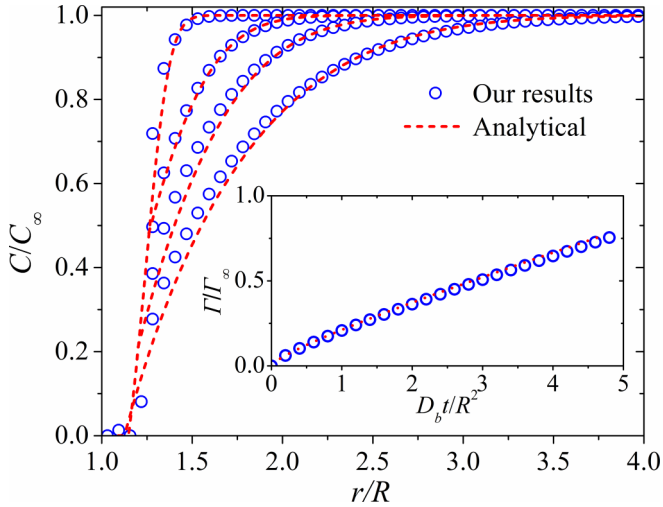

FIG. 2. The diffusion and adsorption test: Bulk surfactant concentration profiles at different times caused by the adsorption in a quiescent fluid with an initial uniform concentration $C = C_\infty$. The desorption term in the bulk surfactant concentration equation is switched off and the source term in Eq. (19) is reduced to $S_\Gamma = k_a C_s$. The inset shows the corresponding surface surfactant concentration at different times. Our results are compared with the analytical results of Muradoglu and Tryggvason [40], i.e., Eqs. (24) and (25).

Length and time are made dimensionless for this test using R and R^2/D_b, respectively. Figure 2 demonstrates that the bulk surfactant concentration and the surface concentration agree well with the analytical solutions of Eqs. (24) and (25), indicating the accurate modeling of the diffusion term and the mass exchange between the bulk liquid and the interface.

The final test case involves bulk surfactant convection as the droplet is displaced by a surfactant solution. The diffusion and source terms in Eq. (18) are switched off, as is the surface surfactant, Eq. (19). The droplet is initially placed at $x = 4$. The values of Ca and λ are 0.1 and 0.05, respectively. Figure 3 shows the indicator function I and the surfactant concentration C near the interface. The droplet obstructs the incoming solution containing the surfactant, causing high convection at the receding contact line and accumulating the surfactant near the front part of the droplet, where a high concentration region is formed. At the droplet interface (i.e., $I = 0.5$), where the bulk surfactant concentration is close to zero, a sharp boundary condition for bulk concentration is imposed. In addition, a correction step is used to eliminate the nonzero mass flux across the droplet surface and the surfactant mass loss is controlled to less than 0.1% over the entire domain [41].

III. RESULTS AND DISCUSSION

This section focuses primarily on the scenario where the droplet is displaced by a surfactant solution. In addition to being influenced by the density, viscosity, surface tension, slip length, and wettability [42,43], the behavior of a droplet can also be categorized according to the relative importance of bulk convection, surface convection, and adsorption rate [44]. In our previous study [38], we investigated the effect of the elasticity number β_s, which is subsequently set as 0.2 and 0.5. The range of surfactant-related parameters is chosen to ensure that the present study can represent all the relevant physical processes associated with the surfactant, including the Marangoni effect, convective-diffusive transport, and surface adsorption and desorption. Therefore, we investigate the range $0.01 \leqslant \mathrm{Bi} \leqslant 10$, $0.1 \leqslant K \leqslant 1$, and $0.01 \leqslant \mathrm{Da} \leqslant 0.5$. All simulations are performed in a domain of $L_x \times L_y \times L_z = 16 \times 4 \times 3$ with a grid resolution of $384 \times 96 \times 72$ and 4608 Lagrangian

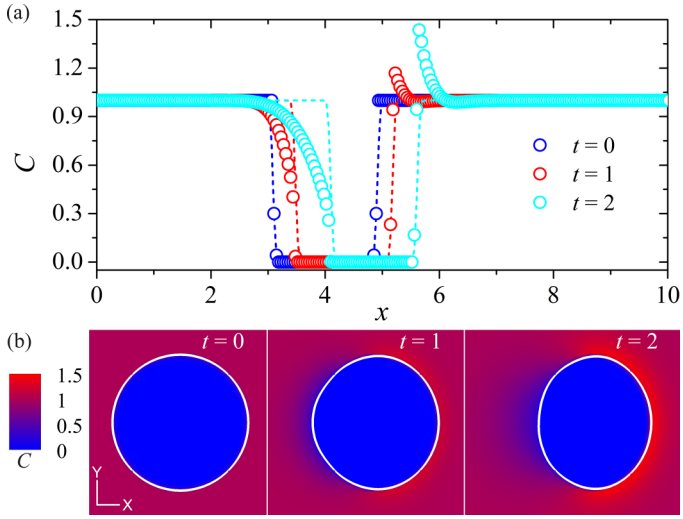

FIG. 3. Bulk convection test. A clean droplet is placed on a solid surface and then suddenly subjected to shear flow with a surfactant solution. The diffusion and source terms in the evolution equation, i.e., Eq. (18), are switched off. (a) The scatter represents the bulk surfactant concentrations C at the center line of the plane $z = 0$ along the x axis at $t = 0$, 1, and 2. The dashed lines represent the indicator function, i.e., $1-I$, which implicitly indicates the location of the interface. (b) The bulk surfactant concentration at the $z = 0$ plane. The white line is the contour $I = 0.5$ showing the contact line.

grids. The deformation parameter D and the displacement velocity U_d are used to characterize the mobility of the displaced droplet, respectively,

$$D = \frac{(L-H)}{(L+H)}, \tag{26}$$

$$U_d = \frac{\int_S u_x \cdot x \cdot \boldsymbol{n} ds}{V}, \tag{27}$$

where L and H are the length and height of the deformed droplet, and u_x and x are the interface velocity and position along the x axis, respectively. In addition, the wetting area A_w is also a key parameter influencing the droplet detachment and it is controlled by the contact-line dynamics and interfacial deformation, both of which are known to have a potentially competing effect on the critical conditions for the onset of droplet detachment [42]. When the droplet undergoes a small deformation along the flow direction, a droplet sliding at a constant velocity and shape is observed. Marangoni effects on the sliding, detachment, and pinching off of droplets covered with insoluble surfactant have been studied in our previous work [38]. The effects of the dimensionless parameters, including the dimensionless adsorption depth K, the Biot number Bi, the Damköhler number Da, and the bulk Peclet number Pe_b, are of particular interest in this paper. We quantify the critical conditions for the onset of droplet detachment, including the critical time t_d and the average surfactant concentration M_s/A, where M_s is the total surfactant mass of surfactant adsorbed on the droplet surface with area A.

As the capillary number Ca rises above a critical value, the wetting area A_w decreases continuously. The contact line becomes unstable and eventually disappears. We examine the effect of surfactant viscosity, i.e., $\mu_\infty/\mu_0 = 1$, 2, and 4, on the droplet displacement. Consistent with the observation for a clean droplet, U_d increases with μ_∞/μ_0 at each given value of Ca. Figure 4 shows droplet snapshots and the time evolution of U_d and A_w for droplets with different values of μ_∞/μ_0. The droplet is displaced until it reaches the steady-state shape at μ_∞/μ_0, at which point U_d and

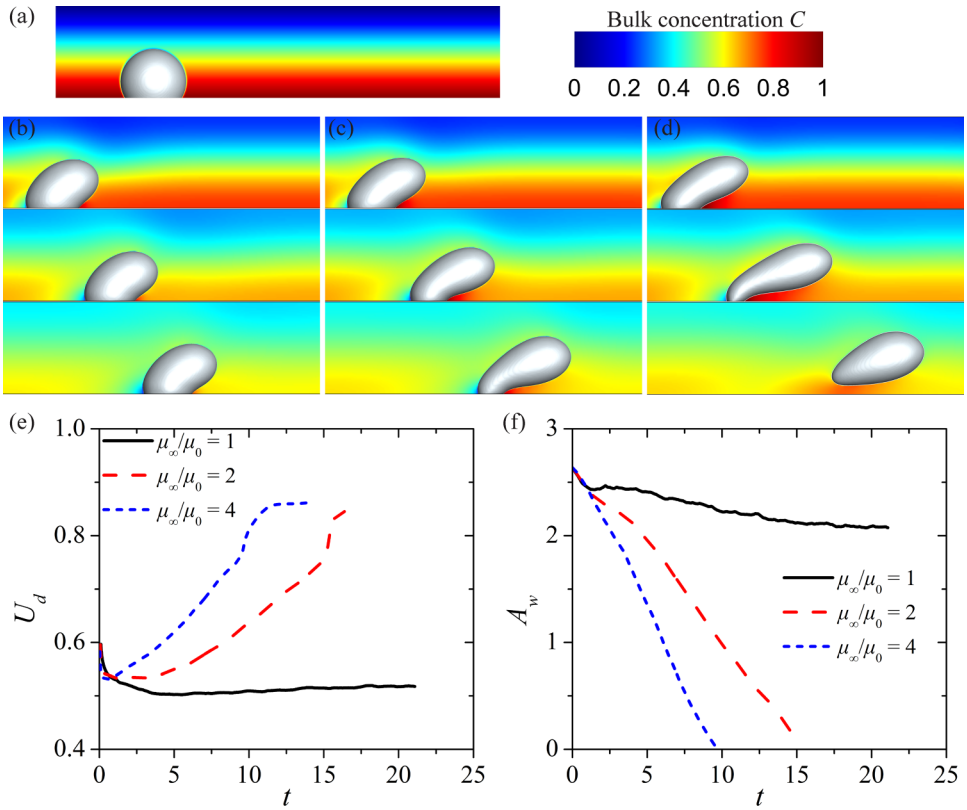

FIG. 4. Distribution of bulk surfactant concentration and the snapshots of the droplet displacement on a solid surface when subjected to a shear flow with a surfactant solution for (b) $\mu_\infty/\mu_0 = 1$, (c) $\mu_\infty/\mu_0 = 2$, and (d) $\mu_\infty/\mu_0 = 4$ at $t = 4$, 8, and 12. For each μ_∞/μ_0, the droplet shape and the bulk concentration C at $t = 0$ are shown in (a). The evolutions of velocity U_d and wetted area A_w enclosed by the contact line are plotted in (e) and (f), respectively. Here, Ca, K, Da, Bi, Pe_b, Pe_s, and β_s are 0.16, 0.1, 0.01, 10, 10, 10, and 0.2, respectively.

A_w become constant. Increased viscosity of the displacing fluid increases the sweeping efficiency, promoting contact-line movement [38]. We increase μ_∞/μ_0 to 2 while keeping all other parameters constant. Following the initial sliding and interface stretching, a neck forms, which gradually elongates with increasing U_d until the droplet finally detaches: the free droplet migrates away from the solid surface and eventually reaches an equilibrium position. When μ_∞/μ_0 is increased to 4, the stretched interface accelerates the disappearance of the wetting area and reduces t_d by 50%, while the critical velocity for detachment remains unchanged. We also plot the bulk concentration in Figs. 4(b)–4(d). The displacing fluid swept up the surfactant in the bulk and accumulates near the advancing contact lines, which becomes more pronounced as μ_∞/μ_0 increases.

To gain further insight into the physical mechanisms underlying the effects of the surfactant on droplet detachment, we present a detailed analysis of the contact-line dynamics for a capillary number below a critical value. As shown in Fig. 5(b), with increasing μ_∞/μ_0, the surface surfactant distribution becomes more nonuniform in the stretching stage. The nonuniform interfacial tension at the advancing contact lines (ACLs) and the receding contact lines (RCLs) dramatically slows down the movement of the contact lines. In addition, the reduced viscous resistance between the droplet and the solid surface accelerates the interfacial deformation, resulting in a rapid disappearance of the contact line. We then examine the effect of K on the contact line at different μ_∞/μ_0. Although surfactant adsorption does not reach an equilibrium, the interfacial dynamics

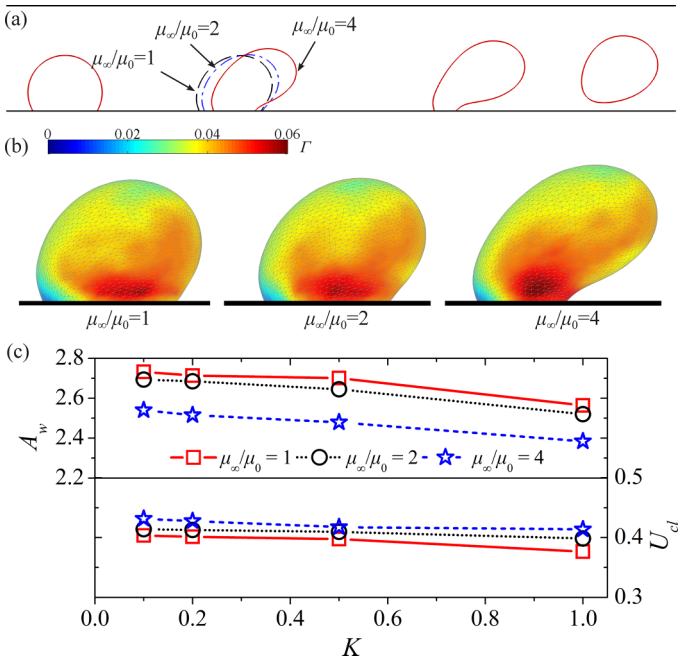

FIG. 5. (a) Snapshots of droplets in surfactant solution with different viscosities, i.e., $\mu_\infty/\mu_0 = 1$, 2, and 4, for Ca = 0.08 and $K = 0.1$ at $t = 0$, 10, 20, and 25. The dashed profiles are steady-state shapes for droplets in surfactant solution with $\mu_\infty/\mu_0 = 1$ and 2, respectively, whereas in the case of $\mu_\infty/\mu_0 = 4$ the droplet finally detaches from the solid surface after the initial sliding. (b) The corresponding snapshots and distributions of the surface surfactant concentration Γ at $t = 10$. (c) The steady-state wetting area A_w and contact-line velocity $U_{\rm cl}$ at different μ_∞/μ_0 for Ca = 0.04. Other parameter values in (a)–(c) are Da = 0.01, Bi = 10, $\mathrm{Pe}_s = 10$, $\mathrm{Pe}_b = 10$, and $\beta_s = 0.2$.

approach a steady state when Ca is below a critical value. As shown in Fig. 5(c), the wetted area A_w decreases with increasing K and is inversely proportional to the net contact-line velocity $U_{\rm cl}$. This decrease in A_w becomes more pronounced at high μ_∞/μ_0. This can be explained by the surfactant-induced nonuniform effects, especially at the interface near the RCLs and ACLs. Consistent with the previous study for the insoluble case [38], the resulting Marangoni stress induces a viscous drag force, thereby promoting the droplet motion. In addition, these nonuniform effects also reduce the wetting area by slowing down the contact-line velocity, which leads to droplet detachment.

In principle, the surface concentration is dominated by the surfactant transfer to the droplet interface and dynamic adsorption, which is enhanced as Bi or K increases. Large K corresponds to a surfactant that is only slightly soluble in the bulk, while small K corresponds to a surfactant that is very soluble. Figure 6(a) shows the steady-state characteristics of the droplet velocity U_d and deformation D for Ca = 0.04. The droplet dynamics is expected to be similar to that of a clean droplet with uniform interfacial tension for small K. U_d increases linearly with K, with a stepped slope at high elasticity numbers. Figure 6(b) shows that the surfactant is adsorbed and accumulates near the ACLs with the interfacial flow. Low interfacial tension reduces the local curvature, offsetting the ACLs advance, especially at high elasticity numbers β_s. This explains the increase in advancing contact angle θ_a and D. As a result, wetting area A_w decreases continuously with increasing K.

Figure 7 presents typical droplet snapshots for four different Biot numbers, 0.01, 0.1, 1, and 10. The promotion of soluble surfactant on detachment is enhanced by increasing the Biot number to 1. When Bi is less than 0.1, the droplet interface continuously and slowly absorbs the surfactant

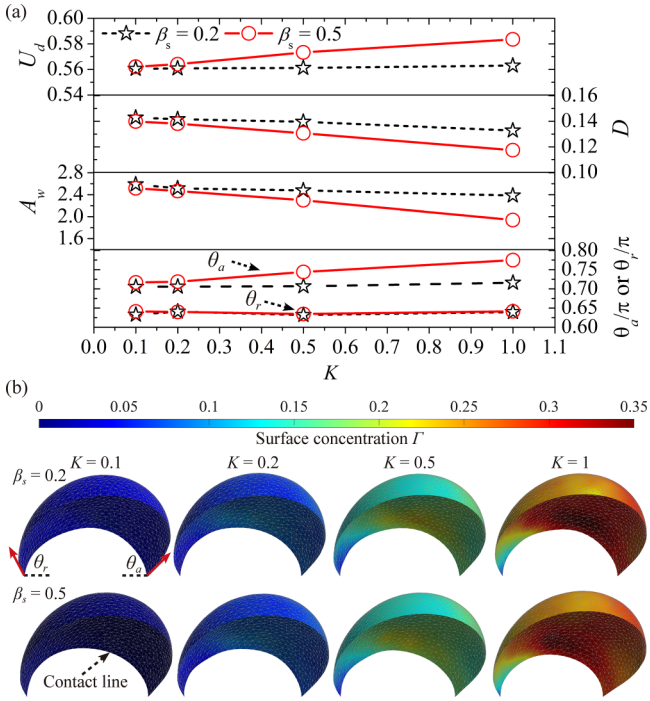

FIG. 6. (a) The displacement velocity U_d and the deformation D of the droplets are plotted as a function of the dimensionless adsorption depth K for different elasticity numbers, i.e., $\beta_s = 0.2$ and 0.5. Color contours are plotted in (b) to show the distribution of surfactant concentration on the droplet surface. Here, Da, Bi, Pe_b, Pe_s, and Ca are 0.01, 10, 10, 10, and 0.04, respectively.

from the surrounding solution. It causes the average surface concentration M_s/A and the difference between the maximum concentration $\Gamma_{\max}$ and the minimum concentration $\Gamma_{\min}$, i.e., $\Gamma_{\max} - \Gamma_{\min}$, to increase continuously until the droplet detaches. A high Bi increases the interfacial kinetic rate of surfactant exchange relative to the interfacial flow rate and enhances solubility transport from the high surface concentration droplet interface into the bulk fluid where surfactant exchange kinetics can rapidly reach equilibrium. Accordingly, the values of M_s/A, $\Gamma_{\max}$, and $\Gamma_{\min}$ initially increase rapidly and then remain constant before detachment. As Bi increases to 10, the enhanced desorption results in a low concentration region near the RCLs. The decrease in $\Gamma_{\max} - \Gamma_{\min}$ before detachment contributes to the increase in t_d, which shows a nonmonotonic tendency with increasing Bi.

In addition to K and Bi, the bulk Peclet number Pe_b controlling the bulk surfactant transport to interface will also affect the droplet detachment. Figure 8 shows the influence of Pe_b on t_d. Other parameters fixed at $K = 1.0$, $\mathrm{Da} = 0.1$, $\mathrm{Bi} = 1$, $\mathrm{Pe}_s = 10$, $\mathrm{Ca} = 0.1$, and $\beta_s = 0.5$, respectively. It is found that t_d shows a nonmonotonic change with Pe_b, and the evolution route can be divided into an enhanced section ($0.1 \leqslant \mathrm{Pe}_b \leqslant 10$) and two stable sections ($\mathrm{Pe}_b < 0.1$ and $\mathrm{Pe}_b > 0$, respectively). The diffusion-controlled transport at $\mathrm{Pe}_b < 0.1$ uniformizes surfactant concentration in the adsorption layer near the droplet surface. The interface behaves more like a clean interface with a uniform interfacial tension. The interface adsorbs surfactant almost uniformly, making it difficult to form a surface tension gradient. Marangoni-induced drag force is less effective in displacing droplets and takes longer to detach. Figure 8(h) shows that at the onset of displacement, the surfactant accumulates at the tip of the droplet, i.e., $\phi \approx 0.2\pi$, and is almost evenly distributed from ACLs (i.e., $\phi = 0$) to RCLs (i.e., $\phi = \pi$). As Pe_b exceeds 10, there is a thin transition layer adjacent to the interface where the bulk surfactant concentration changes rapidly. In addition, the region of

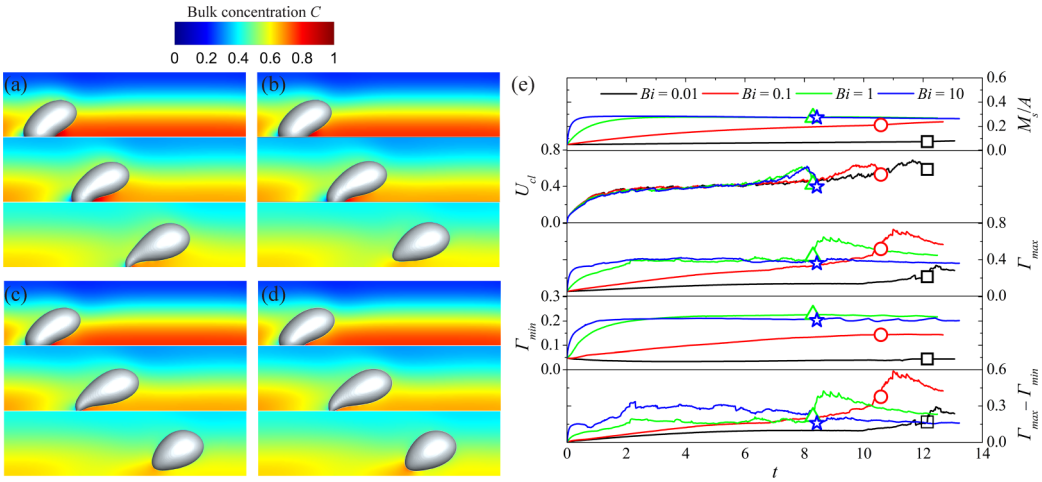

FIG. 7. Successive snapshots of a droplet for the capillary number above the critical value for different Biot numbers, i.e., (a) Bi = 0.01, (b) Bi = 0.1, (c) Bi = 1, and (d) Bi = 10, at $t = 4$, 8, and 12. (e) Time evolution of the average surfactant concentration M_s/A, the average contact-line velocity $U_{\rm cl}$, the maximum $\Gamma_{\rm max}$, and the minimum $\Gamma_{\rm min}$ concentration on the droplet surface. The scatter in (e) shows the moment of detachment and its corresponding critical value. Here, $K = 1.0$, Da = 0.1, $\mathrm{Pe}_s = 10$, $\mathrm{Pe}_b = 10$, Ca = 0.1, and $\beta_s = 0.5$.

high surface concentration begins to move clockwise along the interface until it reaches the ACLs (i.e., $\phi = 0$). Meanwhile, the surface concentration at the RCLs (i.e., $\phi = \pi$) starts to decrease and is even smaller than at the ACLs. This inverse increases the surfactant concentration gradient along the droplet surface, as seen in Fig. 8(h), and the Marangoni-induced drag force thus promotes the droplet detachment. As a result, t_d decreases by 25% as Pe_b increases from 0.1 to 10 in the enhanced section. However, increasing Pe_b up to 10^4 will not increase the drag force any further, and t_d will no longer decrease.

In previous work with high Pe_s number cases, enhanced interfacial convection is found to lower nonmonotonically the critical capillary number for droplet detachment [45]. To fully explain the mechanism of surfactant convection controlling the droplet displacement, we also checked the effect of the Damköhler number. A high Da indicates a fast interfacial exchange rate, while low values indicate that the surfactant exchange is kinetically controlled by convective transport in the surrounding fluid (i.e., high solubility at the interface). Similarly, the enhanced convection with decreasing Da tends to decrease t_d, but the effect becomes progressively weaker (i.e., below 0.05). t_d increases only 6.6% (from 7.48 to 7.97) as Da increases from 0.01 to 0.05. Surprisingly, when Da increases from 0.1 to 0.5, t_d increases up by 36.6%. Figure 9 shows that strong mass exchange downstream from the droplet rapidly reduces the bulk concentration near the droplet surface at high Da. In addition, the concentration gradient within the adsorption layer is essentially negligible due to the low solubility at the interface, and thus the surface concentration is more evenly distributed. The thickened surfactant boundary layer prevents more surfactant from approaching the interface and adsorbing, resulting in a decrease in surface concentration near the ACLs [from Fig. 9(e)], where the increased $u_{\rm cl}$ hinders the reduction in the wetted area and thus slows droplet detachment. In summary, increasing surfactant solubility on the droplet surface enhances surfactant convection to the adsorption layer, thereby promoting the droplet detachment by accelerating the contact-line motion of the ACLs.

The simulations show that detachment is possible when surfactant adsorption produces a surface tension distribution (reduced surface tension and nonuniform induced viscous drag force) that exceeds the critical values. A typical diagram showing the regimes of displacement outcomes and their transition boundary are shown in Fig. 10. We define two dimensionless parameters

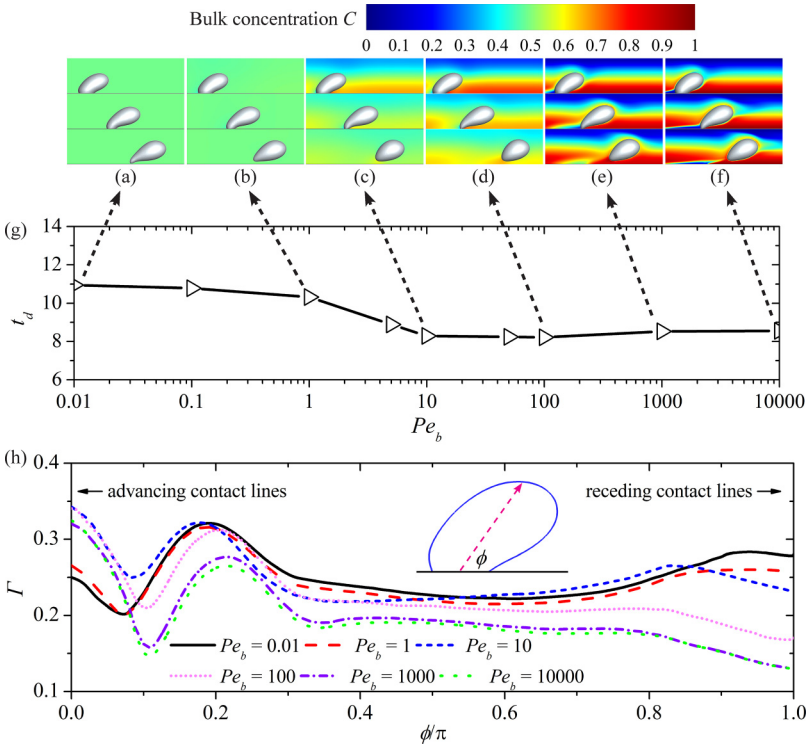

FIG. 8. (g) The critical time t_d for droplet detachment as a function of the Peclet number Pe_b. The corresponding snapshots of the droplet and the distribution of the surfactant concentration in the displacing fluid for (a) $\mathrm{Pe}_b = 0.01$, (b) $\mathrm{Pe}_b = 1$, (c) $\mathrm{Pe}_b = 10$, (d) $\mathrm{Pe}_b = 100$, (e) $\mathrm{Pe}_b = 1000$, and (f) $\mathrm{Pe}_b = 10000$ at $t = 4$, 8, and 11. (h) Surface concentration distribution in the plane of symmetry at $t = 4$. Here, ϕ is the angle between the direction vector of the surface point relative to the wetted center and the x direction. Other parameter values are $K = 1.0$, $\mathrm{Da} = 0.1$, $\mathrm{Bi} = 1$, $\mathrm{Pe}_s = 10$, $\mathrm{Ca} = 0.1$, and $\beta_s = 0.5$.

$\omega = \frac{\mathrm{Bi}\times K}{\mathrm{Da}\times\beta_s}$ and $\xi = \frac{\mathrm{Ca}}{\mathrm{Da}\times\beta_s}$ to present a phase diagram with sliding and detachment conditions. We fixed $\mathrm{Pe}_s = 10$ and $\mathrm{Pe}_b = 10$. Figure 10 shows that as ξ is increased, the droplet is observed to transition from sliding to detachment. When ω was raised while ξ remained constant, significant differences emerged. When ξ is less than 2, any droplet can reach a steady state. Increasing ω does not destabilize the sliding droplet to detach from the solid surface. This is analogous to the cases when ξ exceeds 30, changing ω does not affect droplet detachment. The droplet behavior is sensitive to ω at a moderate value of ξ, i.e., $4 < \xi < 20$. In this range the critical value of ω shows a nonmonotonic change with ξ. Manipulation of the transition from the sliding to detachment can be achieved by increasing ω, but further increases in ω instead delay the droplet detachment. Increasing ω by increasing Bi or decreasing Da will both promote the droplet detachment and reduce t_d. As Da continues to decrease, t_d almost ceases to decrease (see Fig. 9), but further increases in Bi will continue to increase t_d (see Fig. 7) and may even inhibit droplet detachment.

To correlate the detachment dynamics with the surfactant, we define an effective capillary number as $\mathrm{Ca}_e = \mathrm{Ca}/[1 + \beta_s \ln(1 - M_s/A)]$. Figure 11 shows the detachment time t_d as a function of the critical capillary $\mathrm{Ca}_{e,c}$ for droplet detachment. Obviously, t_d decreases sharply and then becomes a constant value with increasing $\mathrm{Ca}_{e,c}$. Surprisingly, for all given values of $\mathrm{Ca}_{e,c}$, we observe that all the data show excellent agreement with a single exponential curve, i.e., $\ln(t_{d,\min} - t_d) \propto \mathrm{Ca}_{e,c}$ where $t_{d,\min}$ is the limit value at $\mathrm{Ca}_{e,c} \to \infty$. The maximum error

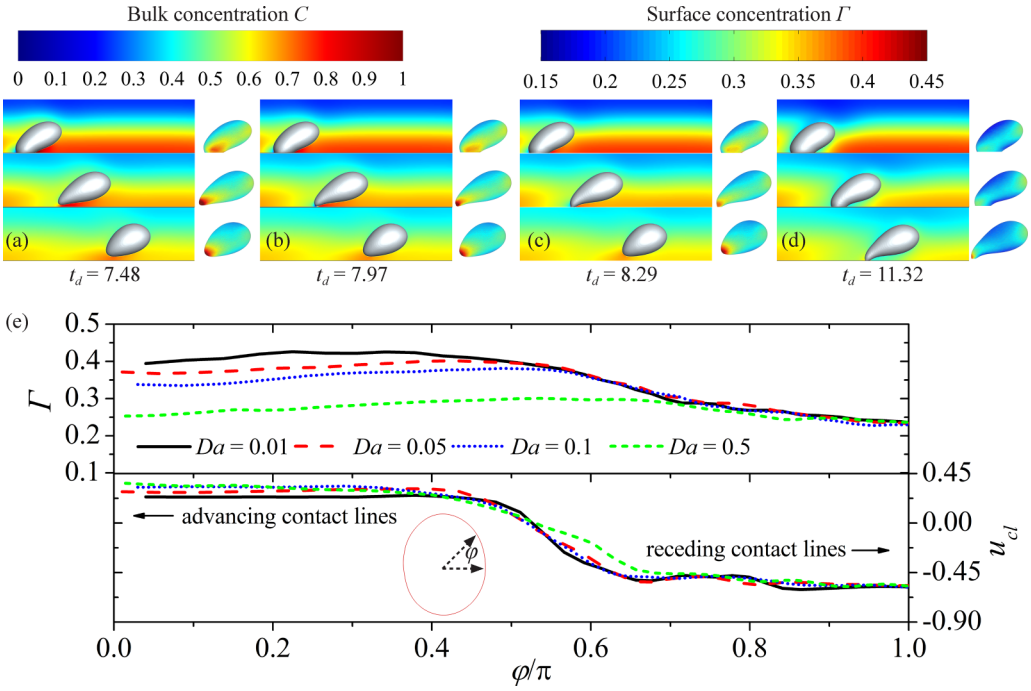

FIG. 9. Distribution of surfactant concentration both in the displacing fluid (left side) and on the droplet surface (right side) for (a) Da = 0.01, (b) Da = 0.05, (c) Da = 0.1, and (d) Da = 0.5. (e) Distributions of the surface concentration and the velocity at the contact line for different Damköhler numbers. The positive and negative signs of u_{cl} mean that the contact lines are advancing and receding, respectively. Other parameters are fixed at $K = 1.0$, $\mathrm{Bi} = 1$, $\mathrm{Pe}_s = 10$, $\mathrm{Pe}_b = 10$, $\mathrm{Ca} = 0.1$, and $\beta_s = 0.5$.

between our data and the curve is less than 15%. The prediction of $t_{d,\min}$ from the curve is 9.71, where the decrease in t_d is less than 1% as $\mathrm{Ca}_{e,c}$ exceeds 0.12. A sliding zone is defined as t_d greater than $10t_{d,\min}$. In this zone, the droplet only deforms but cannot detach from the solid

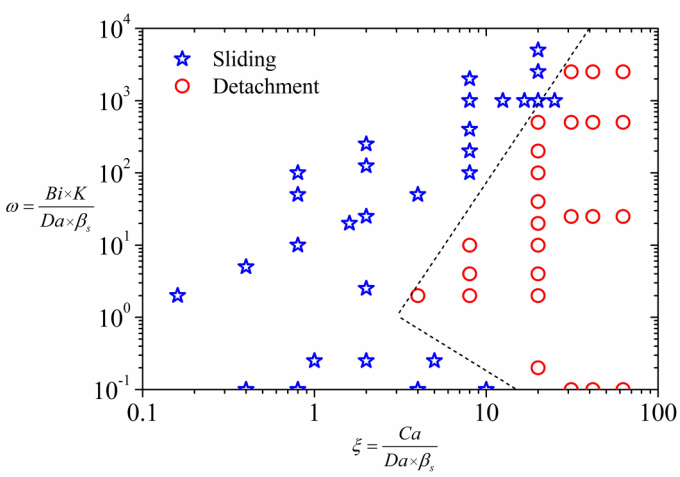

FIG. 10. Effect of parameters that are relevant or specific to surfactant transport on the conditions for droplet sliding and detachment. The fixed parameters are $\mathrm{Pe}_c = \mathrm{Pe}_b = 10$. The dotted line shows the boundary corresponding to the onset of droplet detachment.

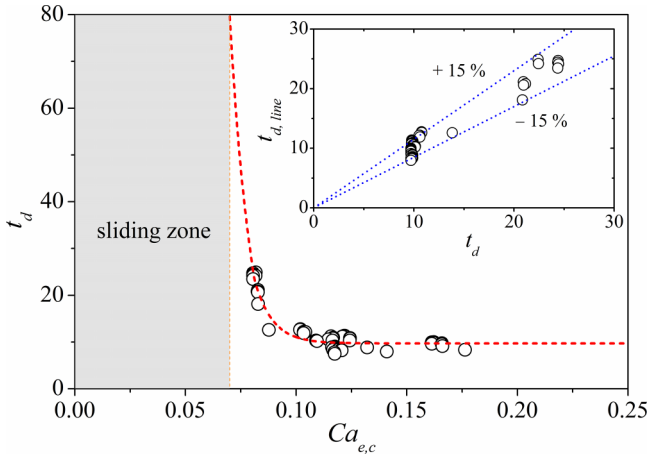

FIG. 11. The detachment time t_d for droplets displaced by surfactant solutions for different critical effective capillary numbers $\mathrm{Ca}_{e,c} = \mathrm{Ca}/(1 + \beta_s \ln[1 - (M_s/A)_c])$, where $(M_s/A)_c$ is the critical value of the average surfactant concentration at the interface at the time of droplet detachment. The fitted curve from our data is represented by the red dashed line. The inset plot shows the upper and lower limits of the relative error between the fitted curve and our numerical data. $t_{d,\mathrm{line}}$ is the value obtained from the fitted curve.

surface until $\mathrm{Ca}_{e,c}$ exceeds the upper limit ($\mathrm{Ca}_{e,c} \approx 0.07$) beyond which the droplet is likely to detach.

IV. CONCLUSION

The primary aim of developing the numerical model described here is to improve our understanding of how droplet displacement on solid surfaces is affected by soluble surfactant-driven flows. The equations for interfacial and bulk surfactant concentration evolution were fully solved by coupling with the two-phase front tracking method to track the soluble-surfactant-laden deformed droplet. The GNBC was adapted here to eliminate the stress singularity near the contact line and to implement a slip boundary linked to the contact angle. We introduced adaptations of the surfactant-dependent front tracking method and GNBC to reconstruct the interface adjacent to the solid surface in a straightforward manner. This approach allows us to explicitly evaluate the position of the contact line, eliminating the need to impose a geometric boundary condition. We validated our method with tests for convection, diffusion, and adsorption cases, finding good agreements between computational results and the analytical solutions. Numerical examples show that our model accurately captures the surfactant transport processes in the bulk and at the droplet interface, allowing the study of surfactant solubility on droplet displacement on the solid surface.

We also performed simulations of a droplet loaded with soluble surfactant moving on a solid surface under shear flow. Consistent with the previous results [38], at low capillary number the droplet eventually reaches a steady deformation and moves at a constant velocity. However, as the viscosity increases, the reduced viscous resistance between the droplet and the solid surface leads to a more nonuniform surfactant distribution on the droplet surface during the initial stretching stage. This nonuniformity increases the deformation of the droplet, making it more prone to detachment, especially at high values of μ_∞/μ_0. Interestingly, an increase in dimensionless adsorption depth K significantly increases the nonuniformity of the surfactant distribution on the droplet surface, which enhances droplet motion due to large Marangoni stresses. Conversely, due to the nonuniform surfactant adsorption on the surface near the contact line, increased surfactant adsorption near the advancing contact line reduces the wetted area with increasing K, resulting in decreased viscous resistance between the droplet and the solid surface. Furthermore, we studied droplet detachment

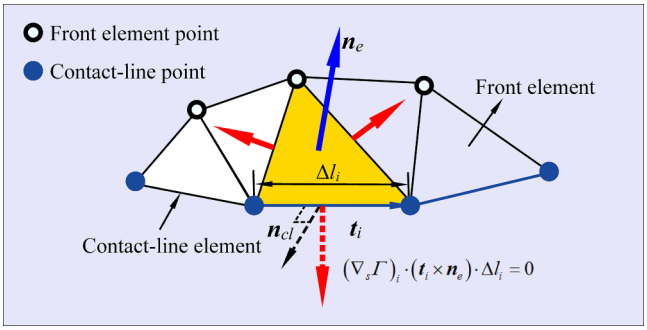

FIG. 12. Implementation of the boundary condition for the surface concentration equation at the contact lines. The yellow triangular element represents the front element adjacent to the contact-line element. $\boldsymbol{n}_e$ is the unit normal of the triangular element and Δl_i and $\boldsymbol{t}_i$ are the length and tangential vector of the contact-line element. $\boldsymbol{n}_{\mathrm{cl}}$ is the normal vector of the contact-line element. The red arrows represent the plane tangential vectors at the midpoints of the three sides of the triangle. The diffusive flux along the tangential vectors (i.e., the dashed arrow) is forced to zero in the equation for the evolution of the surface surfactant concentration.

for varying Bi beyond the critical capillary number and identified the role of surfactants on the critical time t_d for droplet detachment. With increasing Bi, t_d first decreases and then increases, reaching a minimum at Bi $= 1$. At high Bi, rapid equilibrium of surfactant exchange leads to large desorption near the receding contact line. The weakened Marangoni-induced drag forces delay droplet detachment by hindering the motion of the contact line at high Bi numbers. The effect of the bulk Peclet number shows the same trend, but the minimum t_d is reached at $\mathrm{Pe}_b = 10$. Advective surfactant accumulation induces significant Marangoni stress, which ceases to increase with increasing Pe_b. The presence of surfactants always decreases the value of t_d, with the effect being more pronounced at low Da values. To clarify the role of the surfactant solution on the droplet displacement, we defined two surfactant-related dimensionless parameters $\omega = \frac{\mathrm{Bi}\times K}{\mathrm{Da}\times\beta_s}$ and $\xi = \frac{\mathrm{Ca}}{\mathrm{Da}\times\beta_s}$ to identify the onset of the droplet transition from sliding to detachment. ω shows a nonmonotonic effect on droplet detachment due to the nonmonotonic dependence of the Marangoni stress on Bi. To simplify the problem, we defined an effective capillary number Ca_e and correlated it with the critical time t_d for droplet detachment by fitting our numerical data. Surprisingly, t_d can be uniquely described as a single exponential function of the critical value $\mathrm{Ca}_{e,c}$. Under this condition, the limits of $\mathrm{Ca}_{e,c}$ and t_d can be deduced from the fitted curve.

ACKNOWLEDGMENT

This work is financially supported by the National Natural Science Foundation of China (Grants No. 52206212, No. 12272345, and No. 51976160).

APPENDIX A: BOUNDARY CONDITION ON THE SURFACE CONCENTRATION EVOLUTION EQUATION

The diffusion of surfactant between the adjacent elements is assumed to occur at the three edges of the triangle (see Fig. 12). The discrete form of the diffusion term in Eq. (19) is derived as follows:

$$\frac{1}{\mathrm{Pe}_s}\nabla_s \cdot (\nabla_s \Gamma) = \frac{1}{\mathrm{Pe}_s}\left(\sum_{i=1}^{3} (\nabla_s \Gamma)_i \cdot (\boldsymbol{t}_i \times \boldsymbol{n}_e) \cdot \Delta l_i\right). \tag{A1}$$

Here, Δl_i and $\boldsymbol{t}_i$ represent the length and tangent vector of the three edges of the element, respectively. $\boldsymbol{n}_e$ represents the unit normal of the element. The surface gradient$(\nabla_s \Gamma)_i$ can be

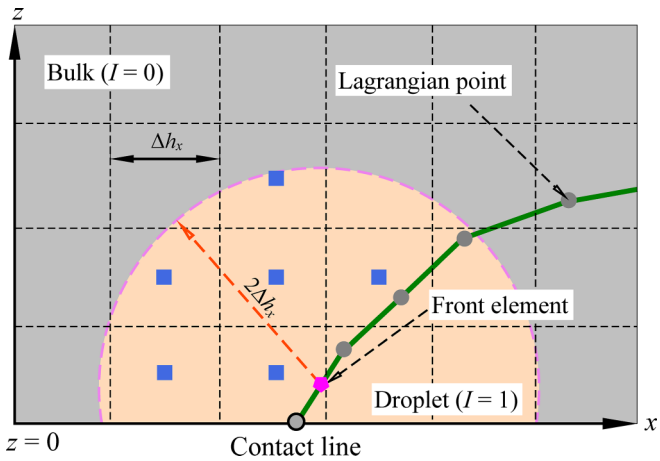

FIG. 13. Normalization of the distribution function. The circle shows the range of action of the distribution function for the front element indicated by the pentagon. The squares (i.e., $I < 0.5$ and $z > 0$) indicate the Eulerian grid points that are involved in the distribution of the source term S_Γ.

obtained by calculating the weighted average of the gradients on the connected triangular elements, taking into account their respective areas. The diffusion flux $(\nabla_s \Gamma)_i \cdot (\boldsymbol{t}_i \times \boldsymbol{n}_e) \cdot \Delta l_i$ is set to zero at the contact lines, as shown in Fig. 12.

APPENDIX B: NON-NORMALIZED DISTRIBUTION FUNCTION

To transfer the front singularities (i.e., surface tension and source term S_Γ) to the fixed Eulerian grid, as suggested by Lai and Peskin [46], the delta function can be approximated using a distribution function $D(\boldsymbol{r})$, which is a tensor product of three one-dimensional discrete forms of the delta

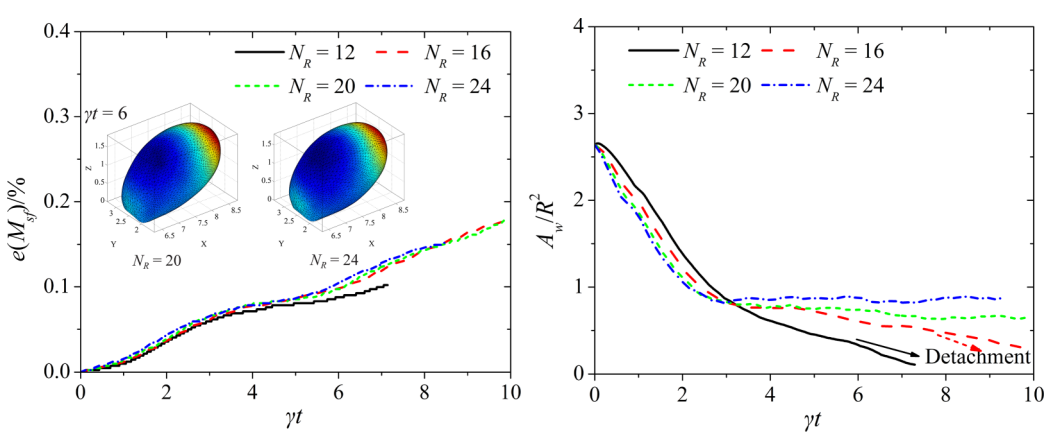

FIG. 14. Convergence study of the surfactant loss $e(M_{sf})$ and wetted area A_w plotted against the dimensionless time γt with different Eulerian grid resolutions at $\mathrm{Ca} = 0.1$, $\mathrm{Pe}_s = 1$, and $\beta_s = 0.4$. Here N_R is the number of Eulerian grids per unit length R. The insets show the color contours on the droplet surface representing the interfacial concentration at $\gamma t = 6$.

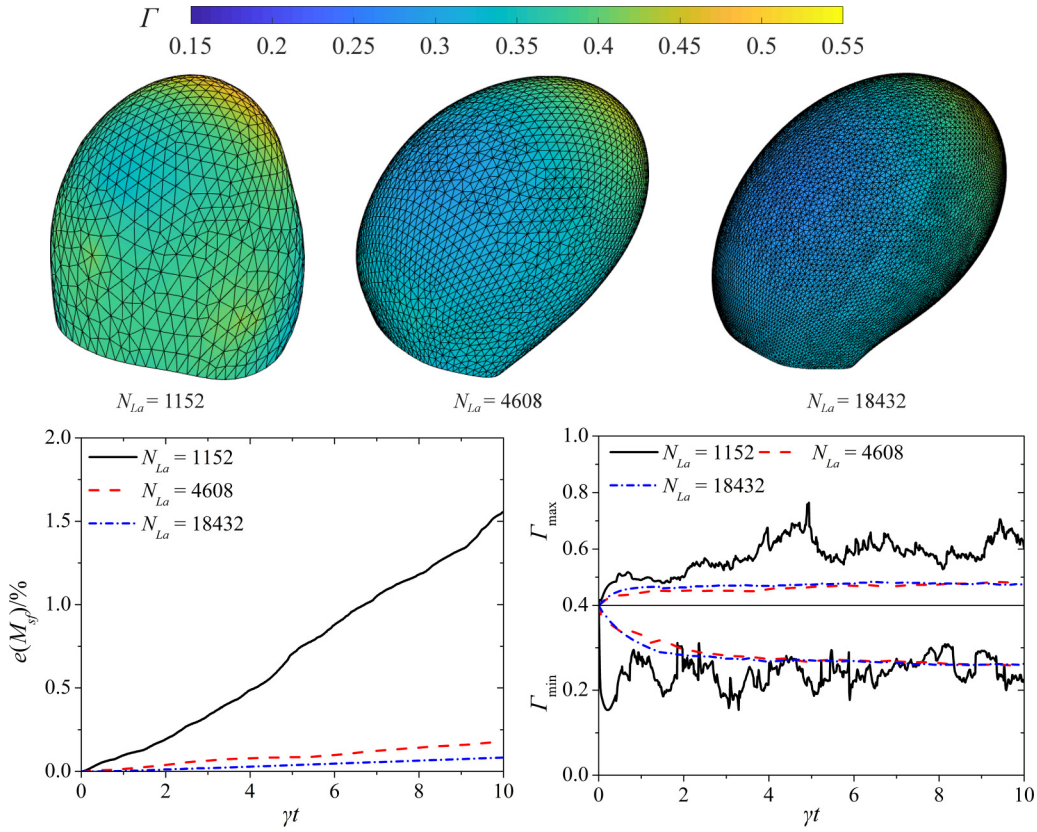

FIG. 15. Convergence study of the surfactant loss $e(M_{sf})$ and interfacial concentration plotted against the dimensionless time γt with different Lagrangian grid resolutions at $\mathrm{Ca} = 0.1$, $\mathrm{Pe}_s = 1$, and $\beta_s = 0.4$. Here N_{La} is the number of Lagrangian grids. The colored contours on the droplet surface represent the interfacial concentration at $\gamma t = 10$.

function,

$$\delta(r) = \begin{cases} \frac{1}{8}(3 - 2|r| + \sqrt{1 + 4|r| - 4r^2}), & |r| \leqslant 1 \\ \frac{1}{8}(5 - 2|r| - \sqrt{-7 + 12|r| - 4r^2}), & 1 < |r| \leqslant 2 \\ 0, & \text{otherwise} \end{cases}. \tag{B1}$$

The non-normalized distribution function can be rewritten as

$$D(\boldsymbol{r}) = \frac{1}{\Delta h_x \Delta h_y \Delta h_z} \delta(r_x)\delta(r_y)\delta(r_z), \tag{B2}$$

where $r_x = (x - x_f)/\Delta h_x$, $r_y = (y - y_f)/\Delta h_y$, $r_z = (z - z_f)/\Delta h_z$, Δh_x, Δh_y, and Δh_z are the Eulerian mesh sizes along the x, y, and z axis, respectively. Due to the presence of the solid surface, the conservation of the physical variable communication between the interface adjacent to the contact line and the Eulerian meshes may not be exactly satisfied. A normalized distribution function is used to ensure the conservation of the body force and continuity of velocity across the contact line [47],

$$D'(\boldsymbol{r}) = D(\boldsymbol{r})/S_f, \tag{B3}$$

where S_f is the sum of the distribution function on the Eulerian meshes above the solid surface (see Fig. 13), and is defined as

$$S_f = \sum_{i,j,k} D(\boldsymbol{r}), \quad \text{if } z > 0. \tag{B4}$$

For the interface far away from the contact line, the consistency condition of the distribution function is satisfied, i.e., $S_f \approx 1$. The distribution function is automatically reduced to a non-normalized form.

APPENDIX C: CONVERGENCE STUDY FOR INSOUBLE CASES

The surfactant is absorbed onto the droplet surface and the surfactant mass exchange between the bulk fluid and the droplet surface is switched. As N_R decreases to less than 20, A_w tends to decrease, and detachment occurs as shown in Fig. 14. The interfacial area of the sliding droplet increases by up to 35% when $N_R > 20$ and the total loss is less than 0.2%. In addition, as N_{La} decreases to less than 4608, $e(M_{sf})$ increases rapidly and exceeds 1.5% (see Fig. 15). After reaching the steady sliding state, the maximum $\Gamma_{\max}$ and minimum $\Gamma_{\min}$ values of the interfacial surfactant concentration fluctuate considerably. As N_{La} increases to 4608, the surfactant loss decreases significantly to less than 0.2%.

[1] B. Bhushan and S. Martin, Substrate-independent superliquiphobic coatings for water, oil, and surfactant repellency: An overview, J. Colloid Interface Sci. **526**, 90 (2018).

[2] L. Thompson, The role of oil detachment mechanisms in determining optimum detergency conditions, J. Colloid Interface Sci. **163**, 61 (1994).

[3] M. Ahmadi and Z. Chen, Challenges and future of chemical assisted heavy oil recovery processes, Adv. Colloid Interface Sci. **275**, 102081 (2020).

[4] D. K. Mandal, A. Criscione, C. Tropea, and A. Amirfazli, Shedding of water drops from a surface under icing conditions, Langmuir **31**, 9340 (2015).

[5] S. Xu, P. Liao, D. Yang, Z. Li, B. Li, P. Ming, and X. Zhou, Liquid water transport in gas flow channels of PEMFCs: A review on numerical simulations and visualization experiments, Int. J. Hydrogen Energy **48**, 10118 (2023).

[6] P. Dimitrakopoulos and J. J. L. Higdon, On the displacement of three-dimensional fluid droplets adhering to a plane wall in viscous pressure-driven flows, J. Fluid Mech. **435**, 327 (2001).

[7] L. He and F. Zhao, Oil–wall interaction induced droplet deformation dynamics in a capillary tube, Phys. Fluids **35**, 082102 (2023).

[8] H. Liu, J. Zhang, Y. Ba, N. Wang, and L. Wu, Modelling a surfactant-covered droplet on a solid surface in three-dimensional shear flow, J. Fluid Mech. **897**, A33 (2020).

[9] S. Wang, S. Chang, H. Zhao, and C. Yang, Dynamic behaviors of water droplet moving on surfaces with different wettability driven by airflow, Int. J. Multiphase Flow **154**, 104127 (2022).

[10] Y. Sui, H. Ding, and P. D. M. Spelt, Numerical simulations of flows with moving contact lines, Annu. Rev. Fluid Mech. **46**, 97 (2014).

[11] A. Mohammad Karim, A review of physics of moving contact line dynamics models and its applications in interfacial science, J. Appl. Phys. **132**, 080701 (2022).

[12] R. Li, R. Manica, Y. Lu, and Z. Xu, Role of surfactants in spontaneous displacement of high viscosity oil droplets from solid surfaces in aqueous solutions, J. Colloid Interface Sci. **579**, 898 (2020).

[13] P. Bazazi and S. H. Hejazi, Retarding spreading of surfactant drops on solid surfaces: Interplay between the Marangoni effect and capillary flows, Phys. Rev. Fluids **5**, 084006 (2020).

[14] A. Nikolov and D. Wasan, Current opinion in superspreading mechanisms, Adv. Colloid Interface Sci. **222**, 517 (2015).
[15] R. Zhao, M. Yu, Z. Sun, L.-j. Li, X.-y. Guo, Y. Xu, and X.-m. Wu, Regulating droplet impact and wetting behaviors on hydrophobic leaves using a nonionic surfactant, J. Colloid Interface Sci. **629**, 926 (2023).
[16] Q. Xie and J. Harting, From dot to ring: The role of friction in the deposition pattern of a drying colloidal suspension droplet, Langmuir **34**, 5303 (2018).
[17] R. G. M. van der Sman and S. van der Graaf, Diffuse interface model of surfactant adsorption onto flat and droplet interfaces, Rheol. Acta **46**, 3 (2006).
[18] H. A. Stone, A simple derivation of the time-dependent convective-diffusion equation for surfactant transport along a deforming interface, Phys. Fluids A **2**, 111 (1990).
[19] I. Seric, S. Afkhami, and L. Kondic, Direct numerical simulation of variable surface tension flows using a volume-of-fluid method, J. Comput. Phys. **352**, 615 (2018).
[20] S. A. Kyle Mahady and Lou Kondic, A volume of fluid method for simulating fluid-fluid interfaces in contact with solid boundaries, J. Comput. Phys. **294**, 243 (2015).
[21] J.-J. Xu, W. Shi, and M.-C. Lai, A level-set method for two-phase flows with soluble surfactant, J. Comput. Phys. **353**, 336 (2018).
[22] O. Tavakkoli, H. Kamyab, M. Shariati, A. M. Mohamed, and R. Junin, Effect of nanoparticles on the performance of polymer/surfactant flooding for enhanced oil recovery: A review, Fuel **312**, 122867 (2022).
[23] A. J. James and J. Lowengrub, A surfactant-conserving volume-of-fluid method for interfacial flows with insoluble surfactant, J. Comput. Phys. **201**, 685 (2004).
[24] Z. Ge, J.-C. Loiseau, O. Tammisola, and L. Brandt, An efficient mass-preserving interface-correction level set/ghost fluid method for droplet suspensions under depletion forces, J. Comput. Phys. **353**, 435 (2018).
[25] M.-C. Lai, Y.-H. Tseng, and H. Huang, Numerical simulation of moving contact lines with surfactant by immersed boundary method, Commun. Comput. Phys. **8**, 735 (2010).
[26] Z. Y. Luo, X. L. Shang, and B. F. Bai, Influence of pressure-dependent surface viscosity on dynamics of surfactant-laden drops in shear flow, J. Fluid Mech. **858**, 91 (2019).
[27] M. Muradoglu and G. Tryggvason, Simulations of soluble surfactants in 3D multiphase flow, J. Comput. Phys. **274**, 737 (2014).
[28] C. Sorgentone, A.-K. Tornberg, and P. M. Vlahovska, A 3D boundary integral method for the electrohydrodynamics of surfactant-covered drops, J. Comput. Phys. **389**, 111 (2019).
[29] K.-Y. Chen and M.-C. Lai, A conservative scheme for solving coupled surface-bulk convection–diffusion equations with an application to interfacial flows with soluble surfactant, J. Comput. Phys. **257**, 1 (2014).
[30] M. Razizadeh, S. Mortazavi, and H. Shahin, Drop breakup and drop pair coalescence using front-tracking method in three dimensions, Acta Mech. **229**, 1021 (2018).
[31] T. Z. Qian, X. P. Wang, and P. Sheng, Generalized Navier boundary condition for the moving contact line, Commun. Math. Sci. **1**, 333 (2003).
[32] S. Ganesan, Simulations of impinging droplets with surfactant-dependent dynamic contact angle, J. Comput. Phys. **301**, 178 (2015).
[33] Y. Yamamoto, S. Higashida, H. Tanaka, T. Wakimoto, T. Ito, and K. Katoh, Numerical analysis of contact line dynamics passing over a single wettable defect on a wall, Phys. Fluids **28**, 082109 (2016).
[34] X. Zhang, J. Zhang, H. Liu, and P. Jia, Rayleigh-Plateau instability of a particle-laden liquid column: A lattice Boltzmann study, Langmuir **38**, 3453 (2022).
[35] M. Zhao and X. Yong, Modeling evaporation and particle assembly in colloidal droplets, Langmuir **33**, 5734 (2017).
[36] X. L. Shang, Z. Y. Luo, E. Y. Gatapova, O. A. Kabov, and B. F. Bai, GNBC-based front-tracking method for the three-dimensional simulation of droplet motion on a solid surface, Comput. Fluids **172**, 181 (2018).
[37] X. L. Shang, Z. Y. Luo, and B. F. Bai, Droplets trapped by a wetting surface with chemical defects in shear flows, Chem. Eng. Sci. **195**, 433 (2019).
[38] J. Zhang, H. Liu, and X. Zhang, Modeling the deformation of a surfactant-covered droplet under the combined influence of electric field and shear flow, Phys. Fluids **33**, 042109 (2021).

[39] M. J. Ni, S. Komori, and N. Morley, Projection methods for the calculation of incompressible unsteady flows, Numer. Heat Transfer, Part B **44**, 533 (2003).
[40] M. Muradoglu and G. Tryggvason, A front-tracking method for computation of interfacial flows with soluble surfactants, J. Comput. Phys. **227**, 2238 (2008).
[41] R. Wang, Nanoparticles influence droplet formation in a T-shaped microfluidic, J. Nanopart. Res. **15**, 2128 (2013).
[42] H. Ding, M. N. H. Gilani, and P. D. M. Spelt, Sliding, pinch-off and detachment of a droplet on a wall in shear flow, J. Fluid Mech. **644**, 217 (2010).
[43] P. Dimitrakopoulos, Deformation of a droplet adhering to a solid surface in shear flow: Onset of interfacial sliding, J. Fluid Mech. **580**, 451 (2007).
[44] Y. Zong, C. Zhang, H. Liang, L. Wang, and J. Xu, Modeling surfactant-laden droplet dynamics by lattice Boltzmann method, Phys. Fluids **32**, 122105 (2020).
[45] X. Shang, Z. Luo, G. Hu, and B. Bai, Role of surfactant-induced Marangoni effects in droplet dynamics on a solid surface in shear flow, Colloids Surf., A **654**, 130142 (2022).
[46] H. Zhang, L. Zhao, J. Mao, and X. Liu, An efficient 3D iterative interface-correction reinitialization for the level set method, Comput. Fluids **213**, 104724 (2020).
[47] H. Zhang, A. Nikolov, and D. Wasan, Enhanced oil recovery (EOR) using nanoparticle dispersions: Underlying mechanism and imbibition experiments, Energy Fuels **28**, 3002 (2014).